Build Simul (2024) 17: 355–370
https://doi.org/10.1007/s12273-023-1097-y

Influence of indoor airflow on airborne disease transmission in a classroom

Mojtaba Zabihi (✉), Ri Li (✉), Joshua Brinkerhoff

School of Engineering, Faculty of Applied Science, University of British Columbia, Kelowna, Canada

Abstract

It has been widely accepted that the most effective way to mitigate airborne disease transmission in an indoor space is to increase the ventilation airflow, measured in air change per hour (ACH). However, increasing ACH did not effectively prevent the spread of COVID-19. To better understand the role of ACH and airflow large-scale patterns, a comprehensive fully transient computational fluid dynamics (CFD) simulation of two-phase flows based on a discrete phase model (DPM) was performed in a university classroom setting with people present. The investigations encompass various particle sizes, ventilation layouts, and flow rates. The findings demonstrated that the particle size threshold at which particles are deemed airborne is highly influenced by the background flow strength and large-scale flow pattern, ranging from 5 μm to 10 μm in the cases investigated. The effects of occupants are significant and must be precisely accounted for in respiratory particle transport studies. An enhanced ventilation design (UFAD-CDR) for university classrooms is introduced that places a premium on mitigating airborne disease spread. Compared to the baseline design at the same ACH, this design successfully reduced the maximum number density of respiratory particles by up to 85%. A novel airflow-related parameter, Horizontality, is introduced to quantify and connect the large-scale airflow pattern with indoor aerosol transport. This underscores that ACH alone cannot ensure or regulate air quality. In addition to the necessary ACH for air exchange, minimizing horizontal bulk motion is essential for reducing aerosol transmissibility within the room.

Keywords

aerosol transmission
airflow pattern
horizontality
COVID-19 simulation
classroom ventilation

Article History

Received: 09 August 2023
Revised: 12 November 2023
Accepted: 22 November 2023

1 Introduction

The recent COVID-19 pandemic has highlighted the significant impact of airborne respiratory disease transmission control in indoor environments. There are different classifications of virus transmission, including human-to-human, airborne, and other ways like endogenous infection, shared vehicle, and vector spread (Morawska 2006). Humans spend most of their time indoors (Klepeis et al. 2001) and even when they are exposed to particles of an outdoor origin, it occurs predominantly indoors (Chen et al. 2012). Particles generated by infected humans can be either directly inhaled or spread from contaminated surfaces (fomites) (Jayaweera et al. 2020). In general, breathing, speaking, coughing, sneezing, and other activities all generate respiratory droplets and aerosols (Anfinrud et al. 2020; Kohanski et al. 2020). In ventilated indoor environments, the ventilation return airflow removes some of the particles, while others may settle on objects or human bodies in the room, and some may be directly inhaled. To reduce airborne disease transmission, measures should be taken to maximize the removal of infectious particles from the environment, while minimizing aerosol inhalation and deposition on people, especially on arms and faces (Morawska et al. 2020; Wang et al. 2021b). It was found that the spread of infectious diseases is related to the distribution of airflow indoors and its circulation pattern (Yu et al. 2004; Zhao et al. 2005; Li et al. 2007; Tung et al. 2009; Gao and Li 2012).

In recent decades, researchers have explored aerosol dynamics and their transport in diverse settings and environments, including an indoor space with dividers and shelves (Vuorinen et al. 2020), two people standing at a

E-mail: Mojtaba.Zabihi@ubc.ca (Mojtaba Zabihi); Sunny.Li@ubc.ca (Ri Li)

distance in a room (Pendar and Páscoa 2020), an isolated room (Tung et al. 2009; Saarinen et al. 2015; Thatiparti et al. 2017; Rogak et al. 2022) a toilet (Li et al. 2020; Li et al. 2023), urban spaces (Hassan and Megahed 2021), a walking person (Tao et al. 2017; Liu et al. 2021), an aircraft cabin (Yan et al. 2009; Yang et al. 2017), other vehicles (Wang et al. 2014; Yang et al. 2022), an operating room (Romano et al. 2015; Wang et al. 2021a), a door opening (Tung et al. 2009; Saarinen et al. 2015; Hendiger et al. 2016), a prayer room (Al Assaad et al. 2019), a classroom (Abuhegazy et al. 2020; Mirzaie et al. 2021; Rencken et al. 2021; Zabihi et al. 2022; Arjmandi et al. 2022; Xu et al. 2023) and many more. However, no study was found to quantitatively relate the large-scale flow pattern to the airborne disease transmission. Furthermore, many simulations, particularly those conducted in university classrooms, were very different in assumptions and implications from a real classroom with people present. For instance, in many studies including those using the Eulerian-Lagrangian approach (Abuhegazy et al. 2020; Mirzaie et al. 2021), the thermal plume from the occupants was neglected, and the unsteady nature of the breathing was also ignored. Instead, these studies obtained the background flow field from steady simulations, followed by Lagrangian particle tracking. Despite its limitations, the Euler-Euler approach was employed by some researchers (Rencken et al. 2021) assuming that pathogens behave similarly to a tracer gas. It is important to note that particles larger than a few microns in diameter behave differently in indoor airflow scenarios compared to gases (Gao and Niu 2007; Li et al. 2013). In addition to these methodological considerations, many studies (Rencken et al. 2021; Arjmandi et al. 2022; Xu et al. 2023) have frequently omitted the complex geometry of the human body in favor of simplifications, as addressing this complexity adds significant work and challenges in creating a suitable numerical grid. However, an experimental study by Zukowska et al. (2012) demonstrated that simplified human geometers, such as cylinders or rectangular shapes, produce considerably more concentrated plumes than those with complex body shapes and do not depict a realistic plume for a human.

In a typical university classroom, back-to-back lecture sessions are held at less than 10-minute intervals. In medical spaces settings, one solution to mitigate the risk associated with Aerosol Generating Procedures (AGPs) is the implementation of an administrative control called fallow time. Following an AGP, a wait-time is undertaken and the medical operatory is left fallow prior to surface sterilization and the next patient being admitted. The fallow time technique assumes that the operatory is equipped with sufficient air change turnover so that around 95% of the aerosols in the air are circulated out during the fallow time (Shahdad et al. 2021). A similar approach can be applied in classroom settings, taking into account ACH and large-scale flow patterns, to evaluate the effectiveness of a 10-minute fallow time in reducing respiratory particle transmission. This research incorporates realistic considerations of human occupants including transient inhalation, exhalation, and natural convection resulting from human body temperature, within an authentic environment. The spatiotemporal evolution of the airflow and respiratory particle transport in a university classroom is simulated to quantify the influence of various ventilation strategies (described in the computational model section) and large-scale flow patterns on aerosol transmission indoors. An enhanced ventilation design for classrooms is introduced which reduces the spread of the aerosols substantially even with lower ACHs compared to the other strategies.

2 Computational model

One of the classrooms in the Engineering, Management, and Education (EME) building at the University of British Columbia's Okanagan campus, EME-1121, served as the basis for establishing the classroom geometry model as depicted in Figure 1. In the actual baseline design two distributed HVAC supplies, large perforated plates on the

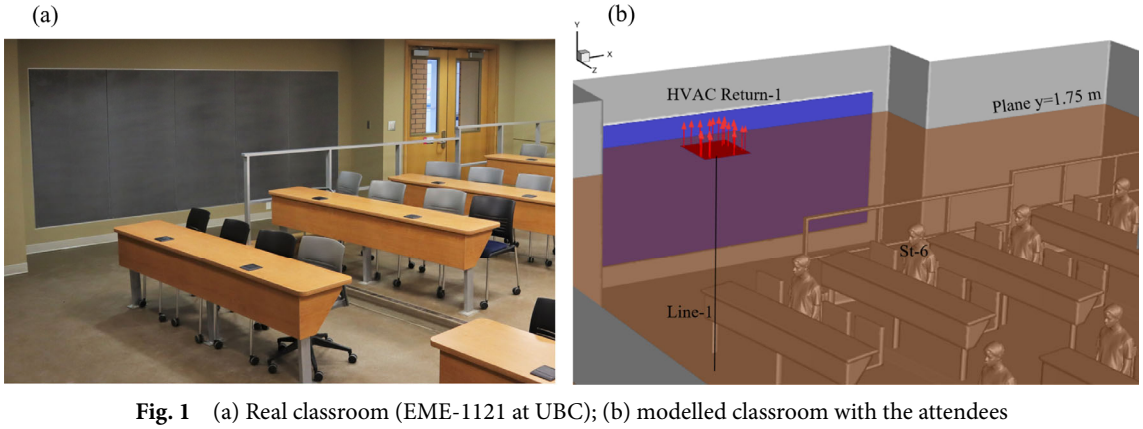

Fig. 1 (a) Real classroom (EME-1121 at UBC); (b) modelled classroom with the attendees

side walls, and two HVAC returns on the ceiling are used to circulate air in the classroom. This design aims for a displacement ventilation (DV) system by supplying air to the classroom from the lower parts of the room at a low, uniform velocity and exhausting it at the ceiling level. More details of the classroom geometry can be found in Figure 2. The HVAC supplies up to 17 ACH for the classroom at a temperature of 17.9 °C and relative humidity of 40%. In the numerical model, all inlet boundaries are set as velocity inlets with 5% turbulent intensity and all outtakes are pressure outlets with zero gauge pressure.

In the modelled classroom, there is a lecturer and 20 socially-distanced students. All 21 individuals in the room are sedentary, and their respiration and heat transfer from their body to the ambient are considered. The clothing is set to a temperature of 28 °C (Zhang et al. 2010; Qingqing et al. 2020), whereas the expected skin temperature for exposed body regions including the head and arms is 34.5 °C (Liu et al. 2013). All other surfaces in the numerical model are assumed to be adiabatic. The transient simulation begins utilizing the steady state data as initial conditions. To replicate a lecture and the break before the start of the following session, the lecturer produces aerosols and droplets for 15 minutes. After the teacher stops producing aerosols, the simulation continues for an additional 30 minutes to monitor the particle dispersion throughout a long fallow period.

Different particle size cut-offs, frequently in the range of 5 μm to 20 μm, have been employed in recent years to classify particles as "aerosols" or "droplets," based on various characteristics of particle behaviors (Leung 2021). To include all particles classified as respiratory aerosols and droplets, this study employs a diverse range of small and large particles (particle diameter from 1 μm to 100 μm) with various number distributions (Morawska et al. 2009; Alsved et al. 2020). For the particles within the respiratory range, evaporation occurs in a very short time making it negligible for the purposes of this study (Chen and Zhao 2010). In this research, the lecturer's mouth emits 272 non-volatile nuclei water particles every second. Particle number distributions for each size are described in Table 1. Particles are assumed to be reflected at the source inlet, exiting the domain if they reach any other inlet or outlet boundaries, and will be permanently removed if they are deposited on the surfaces.

In a relaxed and regular breathing situation, individuals typically spend almost equal durations inhaling and exhaling air. Consequently, in the simulations, each individual follows a sinusoidal rhythm of inhalation and exhalation with a maximum air velocity of 1.63 m/s and a period of 4.05 seconds (Gupta et al. 2010; Phuong et al. 2016). Twenty arbitrary numbers between zero and 4.05 are used to generate random phase-lagged breathing functions for each student. The exhaled humid air has a temperature of 34.85 °C and 90% relative humidity (Morawska et al. 2009), and the opening area of the mouth is 1.84 cm^2 (Gupta et al. 2010).

There are three different airflow strategies (shown in Figure 3) that are taken into consideration: supplies and returns A which is the baseline design aiming displacement ventilation (DV); the second design (supplies A and returns B) which is displacement ventilation with ceiling distributed returns (DV-CDR); and the optimized design (supplies and returns B) which is an under-floor air distribution concept combined with the ceiling-distributed

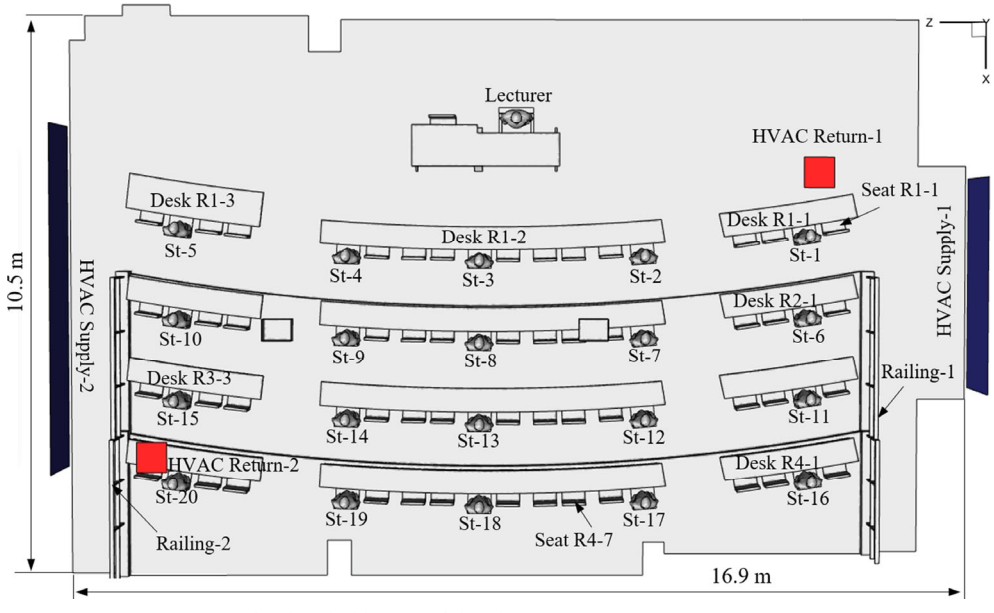

Fig. 2 The detailed layout of the classroom (16.9 m × 10.5 m × 2.6 m)

Table 1 Particles size and numbers

Particle size (μm)	Number of particles/s	Number particles in 15 minutes
1	160	144000
5	60	54000
10	20	18000
20	16	14400
50	12	10800
100	4	3600
Total	272	244800

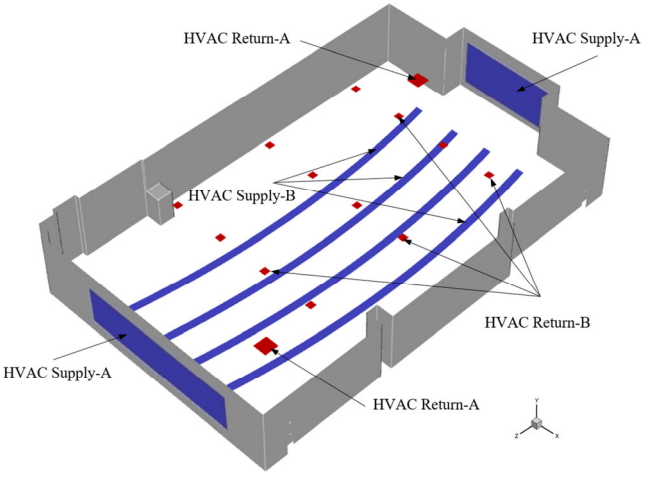

Fig. 3 Airflow configurations in the classroom; supplies and returns A: DV; supplies A and returns B: DV-CDR; supplies and returns B: UFAD-CDR

returns (UFAD-CDR). To investigate the impact of airflow in the classroom, full load (maximum ACH) and half load (half of the maximum ACH) ventilations have been simulated for each of the layouts. Additionally, a simulation has been performed to investigate how the thermal plume produced by humans impacts particle transport in the classroom. All conditions in this case are identical to the baseline design with full HVAC load, unless the skin and clothing are adiabatic surfaces. Two more simulations were run to compare the efficacy of the UFAD-CDR ventilation to the baseline DV when, instead of the lecturer, one of the students (St-8) in the middle of the classroom produces pathogens.

3 Governing equations

The flow to be modelled has two phases: a continuous phase and a discrete phase. The continuous phase is the gas flow, which is considered as a binary mixture of air and water vapour. Hereinafter, we will call it the continuous phase airflow, while the water vapour content in the air determines the relative humidity. The discrete phase is the droplets emitted from the human's mouth. There are multiple flow sources in the room (HVAC supplies, particle flows, and human breathing flow) with different temperatures and relative humidity. As a result, the transports of energy and species, in addition to momentum transfer, must be solved.

A fully transient Euler-Lagrange approach in ANSYS-Fluent is applied, utilizing the Lagrangian discrete phase model to track particles. This methodology is commonly used when interactions between droplets can be neglected as the discrete phase is assumed to be diluted enough.

Considering the many models provided by ANSYS-Fluent for turbulence calculations, k-ε and k-ω models are more practical for such a large computational domain since DNS and LES with a proper grid size and time steps are extremely costly. Among k-ε and k-ω models, the RNG k-ε (Chan et al. 2002; Tominaga and Stathopoulos 2009), realizable k-ε (Yu and Thé 2017; Liu et al. 2020), and SST k-ω (Ramponi and Blocken 2012) turbulence models have been recommended by other studies because of their theoretical superiority to the other k-ε and k-ω models for these applications. For particle-laden turbulence simulations, SST k-ω has shown better agreement with DNS and experimental data as a result of its shorter Lagrangian integral time scale than the RNG k-ε model (Gao et al. 2012). SST k-ω also predicted particle deposition with a better agreement to LES and experimental data than realizable k-ε (Tang et al. 2015). Therefore, in the present work, the SST k-ω turbulence model is employed for the closure of unsteady Reynolds averaged Naiver-Stokes (URANS) equations.

The continuity and momentum equations for the continuous phase are the URANS equations described in Equations (1) and (2).

$$\frac{\partial \rho}{\partial t}+\frac{\partial(\rho u_i)}{\partial x_i}=0 \tag{1}$$

$$\frac{\partial(\rho u_i)}{\partial t}+\frac{\partial(\rho u_i u_j)}{\partial x_j}=\rho g_i-\frac{\partial p}{\partial x_i}+\mu\frac{\partial}{\partial x_j}\Big(\frac{\partial u_i}{\partial x_j}+\frac{\partial u_j}{\partial x_i}-\frac{2}{3}\delta_{ij}\frac{\partial u_l}{\partial x_l}\Big)+\frac{\partial}{\partial x_j}\Big(-\rho\overline{u_i' u_j'}\Big) \tag{2}$$

in which ρ is the fluid density, u and u' with i, j, or l subscripts are the three components of the mean and fluctuating velocities, p is the pressure, and μ is the molecular viscosity. The term $\left(-\rho\overline{u_i' u_j'}\right)$ in Equation (2) is the Reynolds stress tensor that is being modelled by the SST k-ω turbulence model. The SST k-ω equations are well described in the literature (Abrahamson 2021).

The convective heat transfer equation for the continuous phase is

$$\frac{\partial(\rho E)}{\partial t}+\frac{\partial\left[u_i(\rho E+p)\right]}{\partial x_i}=\frac{\partial}{\partial x_j}\left(k_{\text{eff}}\frac{\partial T}{\partial x_j}\right)+S_{\text{h}} \tag{3}$$

In Equation (3) E is the total energy of the fluid, k_{eff} is the effective thermal conductivity, T is the continuous phase temperature, and S_{h} is the heat being transferred between the continuous and discrete phases.

Particles are tracked in the Lagrangian frame of reference, and the particle motion is governed by:

$$\frac{\mathrm{d}\vec{u}_{\text{p}}}{\mathrm{d}t}=\frac{\vec{u}^{\text{INST}}-\vec{u}_{\text{p}}}{\tau_{\text{r}}}+\frac{\vec{g}\left(\rho_{\text{p}}-\rho\right)}{\rho_{\text{p}}} \tag{4}$$

where $\vec{u}^{\text{INST}}$ is the continuous phase instantaneous velocity, $\vec{u}_{\text{p}}$ is the particle velocity, ρ_{p} is the density of the particle, and τ_{r} is the particle relaxation time.

The turbulent dispersion of particles is predicted by integrating the motion equations for all of the individual particles, utilizing the instantaneous fluid velocity as expressed below:

$$u_i^{\text{INST}}=u_i+u_i' \tag{5}$$

Here u_i represents the three components of $\vec{u}$, and the average velocity of the fluid u_i is obtained by the URANS equations. Based on a stochastic method called eddy lifetime or the discrete random walk (DRW) model, the fluctuating component u_i' is assumed to be isotropic and to follow a Gaussian distribution, which can be obtained from Equation (6):

$$u_i'=\zeta\sqrt{\frac{2}{3}k} \tag{6}$$

where ζ is a random number with a normal distribution and k is the turbulent kinetic energy predicted by the turbulence model. The concept of the fluid Lagrangian integral time scale τ_{L}, which describes the duration of turbulent motion along the particle path, is used in the prediction of particle dispersion with small drift velocities. For SST k-ω, this time scale can be approximated as:

$$\tau_{\text{L}}=\frac{1.67}{\omega} \tag{7}$$

where ω is the specific dissipation rate of turbulent kinetic energy.

There is a straightforward heat balance equation that connects the particle temperature $T_{\text{p}}(t)$, to the convective heat transfer:

$$m_{\text{p}}c_{\text{p}}\frac{\mathrm{d}T_{\text{p}}}{\mathrm{d}t}=hA_{\text{p}}\left(T_\infty-T_{\text{p}}\right) \tag{8}$$

where c_{p} is the particle heat capacity, A_{p} is the particle surface area, T_∞ is the local temperature of the continuous phase, and h is the convective heat transfer coefficient.

For solving Equations (1)–(3), the coupled algorithm is employed for the pressure–velocity coupling. The gradients, pressure, and diffusion terms are discretized with second-order accuracy, while convection terms are discretized using the second-order upwind scheme. The transient formulation is being solved with 0.5 second time steps in a first-order implicit way. Discrete phase equations are solved using the high-resolution unsteady tracking method and implicit-trapezoidal discretization scheme (Abrahamson 2021). The time step employed in solving the position of the discrete phase is limited such that the average particle displacement in each time step is less than 0.5 mm.

In this study, flow parameters such as vorticity, $\vec{\Omega}$, helicity, H, and enstrophy, Ω^2, were investigated as potential parameters for quantifying large-scale flow patterns and relating it to particle concentration in a room. Vorticity, helicity, and enstrophy are defined in Equations (9) to (11) respectively.

$$\vec{\Omega}=\vec{\nabla}\times\vec{u} \tag{9}$$

$$H=\vec{\Omega}\cdot\vec{u} \tag{10}$$

$$\Omega^2=\vec{\Omega}\cdot\vec{\Omega} \tag{11}$$

4 Spatial grid and validation

Grid generation is accomplished using Ansys-Meshing software. To discretize the geometry of the model, a multi-grid mesh, with a 20-layer structured prism inflated grid for the boundary layer and a tetrahedral unstructured mesh for the bulk flow were used. The grid has to be adequately resolved to capture the natural convection surrounding a human body. Numerous mesh sizes have been used on the intricate complex human geometry and its surrounding computational domain. The minimum, maximum, and average y+ value for the wall-adjacent cells are 0.005, 15.1, and 0.52, respectively.

The grid study is carried out with five different meshing resolutions to ensure that the impacts of grid size on the simulation's results are minimal. On a cut-through plane at 1.75 m height from the floor, volumetric flow rate, maximum velocity magnitude, and average-vorticity magnitude are examined and compared as the grid study parameters for different meshing resolutions in Table 2. In comparison to the other cases, the relative differences (RD) between the studied parameters for the cases of 40.35M and 30.24M elements are within an acceptable range of 1%. Therefore, in order to lower processing costs and time requirements, grid sizes of 30.24M elements are employed for the simulations. The relative difference formula is defined in

Table 2 Grid study summary

Case	40.35M	30.24M	27.18M	21.08M	14.8M
Volumetric flow rate (m^3/s)	1.868	1.867	1.871	1.830	1.814
% Relative difference	0.05	0.21	2.19	0.87	—
Maximum velocity magnitude (m/s)	0.409	0.412	0.402	0.374	0.345
% Relative difference	0.73	2.42	6.96	7.75	—
Average-vorticity magnitude (s^{-1})	0.259	0.260	0.263	0.248	0.236
% Relative difference	0.39	1.15	5.70	4.84	—

Equation (12), where x_1 and x_2 are the new and initial values obtained for two consecutive grids:

$$RD = \frac{|x_1 - x_2|}{x_2} \times 100 \quad (12)$$

To validate the numerical model, the velocity profile in the real classroom at the line-1 location was measured using a hand-held hot wire (Dwyer 471B-1, ±3% FS) and compared with the CFD results (Figure 4). As depicted in Figure 1, Line-1 runs vertically from the centroid of HVAC-Return-1 to the floor. Despite the fact that the maximum measured velocity is lower than the simulated velocity, the simulated velocity profile still agrees well with the experimental data. The actual flow rate may be lower than the designed value because the classroom is not airtight and the return flow rate may be lower than the supplied air. However, in the low-velocity range, the accuracy of the hand-held hot wire may be adversely affected by the presence of the operator and the precision of the sensor but still, a good match is observed within this velocity range.

5 Results and discussion

The flow field and particle distribution in the lecturer's close proximity as well as the effects of the thermal plume, airflow strategies, and particle source location on the spread of airborne disease in the classroom, are discussed in the following subsections.

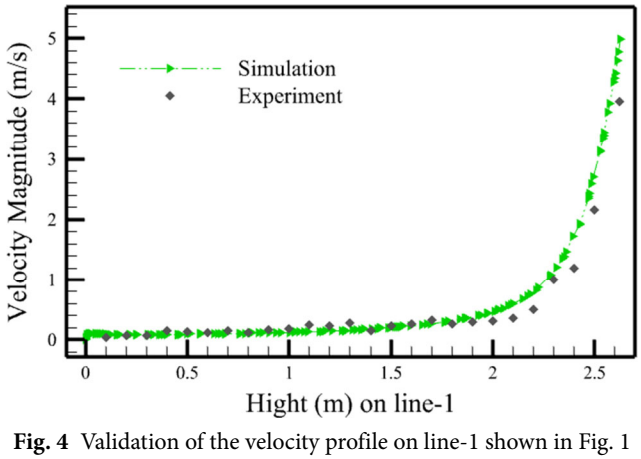

Fig. 4 Validation of the velocity profile on line-1 shown in Fig. 1

5.1 Flow field and particle behavior around an individual

The contours of the airflow characteristics, such as velocity magnitude, relative humidity, density, turbulent kinetic energy, and static temperature, are shown in Figures 5(a)–(e) respectively to help understand the flow field around a person. The contours demonstrate how these parameters are distributed along two perpendicular cutting planes showing the lecturer's right profile and front view. The natural convection-driven flow that surrounds the lecturer is substantially stronger than the background flow created by HVAC air circulation. The velocity magnitude over a person's shoulders can be up to 10 times greater than its value in areas where buoyancy forces are not present (Figure 5(a)). The annular boundary layer developing on the torso converges and merges above the shoulders and head where the velocity reaches its local maximums. The velocity contours are in good agreement with the accepted experimental data available in the literature (Li et al. 2018). The maximum velocity values could be slightly different depending on the body size and temperature gradients. As expected, the density and relative humidity are lower around the body where the static temperature is higher. In the random walk model, the reconstruction of the fluctuating part of the velocity field and particle dispersion in the environment relies on the turbulent kinetic energy. As illustrated in Figure 5(d), the turbulent kinetic energy significantly increases around the lecturer compared to outside the thermal plume. The turbulent kinetic energy peaks when the warm body's plume shears and slows into the surrounding air.

Figure 6 illustrates the exhaled particle distribution after 5 seconds, coloured by particle residence time (Figure 6(a)), particle diameter (Figure 6(b)), and particle velocity (Figure 6(c)). For such a flow condition (close to the lecturer affected by the thermal plume), the particles respond differently depending on their size and location. The 100 μm particles fall immediately. Their trajectory is mainly governed by their initial momentum and gravity. Small particles (1, 5, and 10 μm) behave like aerosols at this moment. The gravitational forces are negligible in comparison to the drag forces which are the main determinants of the aerosols' motion. 20 μm particles are slightly slower than the smaller ones but still follow the airflow direction. From the particle velocities (Figure 6(c)), it can be seen that the velocity magnitude for the majority of the 50 μm particles is within a very low range. Some have been dragged up but most of them settle with a very low velocity. This observation suggests that the drag and gravitational forces acting on

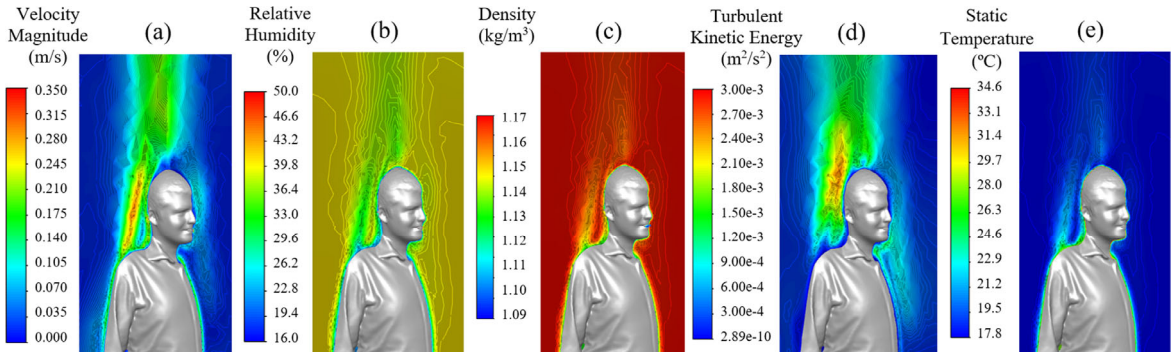

Fig. 5 Contours of airflow parameters around the lecturer: (a) velocity magnitude; (b) relative humidity; (c) density; (d) turbulent kinetic energy; and (e) static temperature

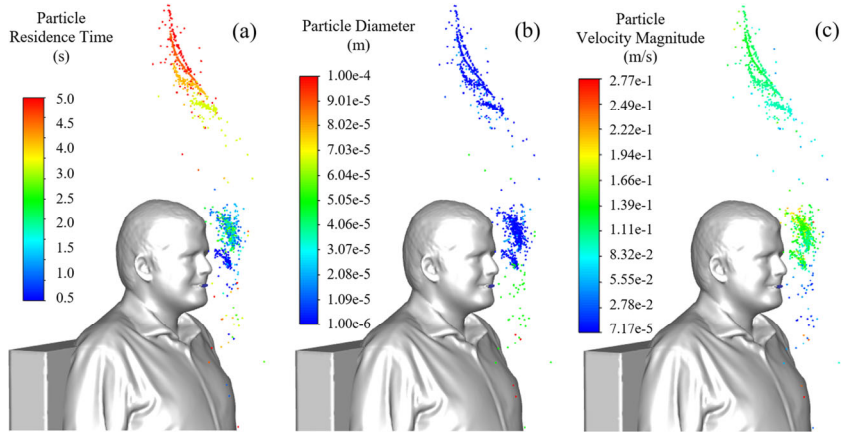

Fig. 6 Particle distributions at t = 5 s, coloured by (a) particle residence time; (b) particle diameter; (c) particle velocity

50 μm particles are nearly balanced at the start of their motion. The 50 μm particles fall and accelerate toward the ground under the dominance of gravitational forces when they approach the region less affected by the thermal plume.

5.2 Thermal plume effect

The velocity magnitude in a thermal plume can reach ten times its value outside of the bouncy affected reign as illustrated in Figure 5(a). As a result, when the thermal plume is not included in the simulation, the particle distribution is drastically altered. Figure 7 compares particle distributions after one minute of emission for three scenarios with different levels of thermal plume effects, including plume generated by body heat and exhalation (Figure 7(a)), exhalation only (Figure 7(b)), and no plume (Figure 7(c)). In the case of a full thermal plume, the particles are carried upwards by the plume and eventually form a thin cloud near the ceiling (Figure 7(a)). In the absence of a body thermal plume, the particles are carried by the exhaled air, which has a higher temperature than the surrounding air. Although it still rises, its momentum quickly dissipates into the air around it. The particles form a cloud which is not as thin as it would be in the presence of a full thermal plume

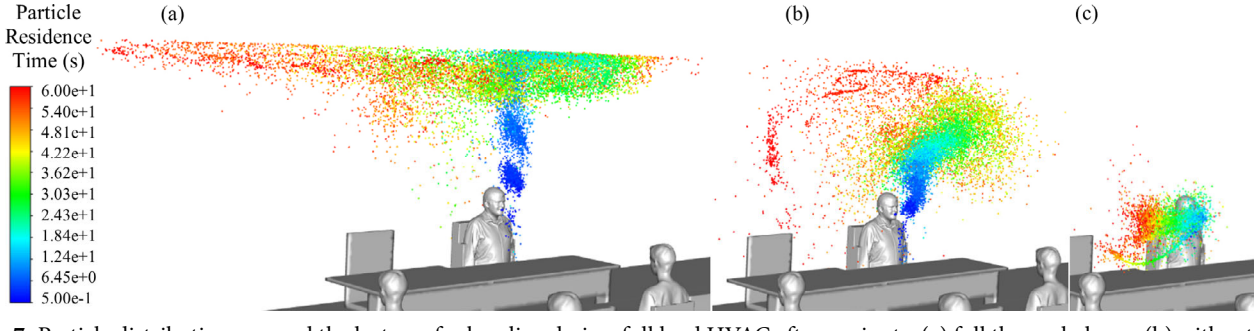

Fig. 7 Particle distributions around the lecturer for baseline design-full load HVAC after a minute: (a) full thermal plume; (b) without the body plume; (c) no thermal plume

and it remains at a lower elevation close to the lecturer. When the heat from exhalation was also excluded, the particles propagated in a completely different pattern that followed the background flow produced by HVAC.

The particle clouds are characterized using the average elevation of the particles, and the area of dispersion, calculated assuming it conforms to an elliptical shape projected on a horizontal plane. The average upward velocity component within a sphere (0.5 m in diameter) around the lecturer's head is also compared across the three cases in Table 3. The stronger thermal plume accelerates the spread of particles and also leads them to be positioned at higher elevations at the early stage of the spread. The substantial difference between the particle clouds and the velocity filed around an individual in the three cases highlights the need to consider the significant effect that human presence has on aerosol transmission in a room.

5.3 Airflow strategies

As described in Figure 3, three ventilation configurations were considered; the baseline (DV), second (DV-CDR), and optimized (UFAD-CDR) designs. Two flow rates (full load and half load) are studied for each of the designs. The full load state is when the HVAC system is operating at its maximum capacity. The room's HVAC system will modify the flow rate based on the number of students in the classroom. In actual use, it typically runs at a point between 50% and 100% load. Half load for this particular classroom provides 8.5 ACH, which is still considerably greater than the designs for normal classrooms in most buildings (2–5 ACH).

A performance comparison of the three ventilation layouts at 17 and 8.5 ACHs is provided in Figure 8. The overall particle number densities over time for each of

Table 3 Particle clouds and velocity field around the lecturer for three thermal effect levels

Thermal plume level	Area of spread (m^2)	Average particle elevation from the source level (cm)	Average upward velocity around the head (m/s)
Full thermal plume	20.32	112	0.071
Without the body plume	8.01	58	0.0049
No thermal plume	3.04	−4	−0.0013

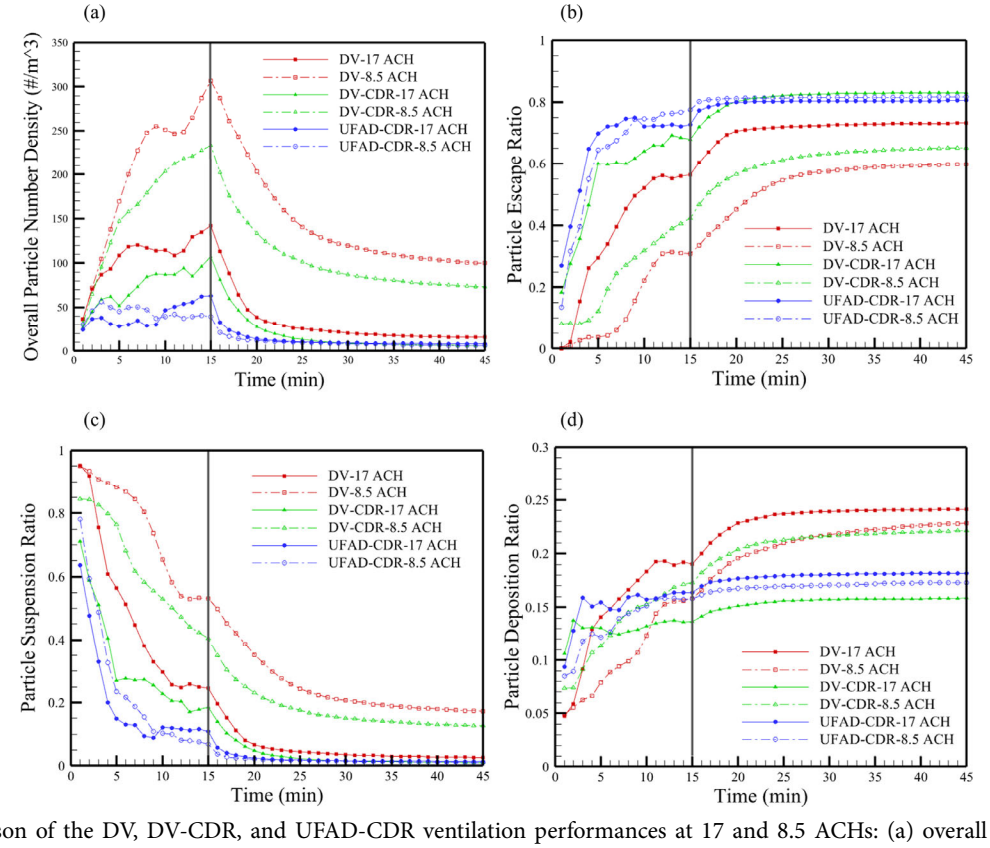

Fig. 8 Comparison of the DV, DV-CDR, and UFAD-CDR ventilation performances at 17 and 8.5 ACHs: (a) overall particle number density; (b) particle escape ratio; (c) particle suspension ratio; (d) particle deposition ratio

the six simulated scenarios are shown in Figure 8(a). The overall particle number density is calculated by dividing the total particle counts still present in the classroom by the volume of the entire computational domain. The plots of the ratios of escaped, suspended, and deposited particles to all emitted particles at the relevant time can be found in Figures 8(b)–8(d). The overall particle number density and particle ratios are significantly influenced by the ventilation layout. ACH has a major impact on the DV and DV-CDR results. In these cases, a higher ACH improves particle removal by the HVAC system. The situation in the classroom has improved for the DV-CDR but still, almost 15% of the particles are in the room after 30 minutes of fallow time in the half load scenario which is not a significant decline in comparison to 20% for the baseline design. However, the results for the UFAD-CDR have substantially altered. Only less than 2% of the particles are still suspended in the room after 10 minutes of fallow time (Figure 8(c)). The results show that having a 10-minute break does not guarantee that the next lecture will begin in a safe classroom unless the ventilation strategy and ACH are properly chosen. When UFAD-CDR ventilation is used, the ACH has only a minor effect on the air quality in the classroom. The suspension ratio illustrated in Figure 8(c) meets the acceptable fallow time criteria of 10 minutes only for DV-CDR at 17 ACH and UFAD-CDR at both flow rates. The maximum particle number density for the optimized design has dropped by 85% and 78% at half load and by 64% and 54% at full HVAC load, in comparison to its values for the baseline and second designs respectively. For each case, the deposition ratio slopes gently throughout the emission time and stabilizes between 10% and 20% after 10 to 15 minutes of fallow time (Figure 8(d)).

In order to demonstrate how the particles are distributed in the height direction of the classroom, the computational domain is divided into 26 slices that are each 10 cm in height. The cumulative particle number density, $n_c(y)$ is calculated by integrating the average particle number density, $\overline{n_s}(i)$ within the i^{th} volume slice at the mid-height of it in the room height direction, y, where N_i is the i^{th} volume:

$$n_c(y) = \sum_{i=1}^{N_i} \overline{n_s}(i) \tag{13}$$

The cumulative particle number densities for the baseline (DV) and optimized (UFAD-CDR) designs at t = 10 and 25 minutes are shown in Figure 9. The vertical axis represents the non-dimensional height normalized with room height, y/h_R. At t = 10 minutes, a high particle concentration is observed near the ceiling in the baseline design for both full and half load cases. In comparison to the DV, the cumulative particle number density in the UFAD-CDR is substantially lower along the classroom height for both full and half HVAC loads. Although the cumulative particle number density for the UFAD-CDR still increases over the room height, there is no highly concentrated region near the ceiling as there is for DV. When the bulk flow circulates at a lower ACH, the drag forces acting on the particles are smaller, which causes them to have a stronger tendency to sediment and settle near the floor. As a result, once the particles have had enough time to settle at 8.5 ACH, a high particle number density zone towards the floor is formed in both configurations (Figure 9(b)). In a displaced ventilated room, while the boundary layer develops around a sedentary human, it transports and induces air from the lower parts of the room and brings it up to the breathing zone (Brohus and Nielsen 1996). The results shown in Figure 9(b) indicate that a higher ACH would aid in having a safer environment for longer settings when people are sedentary.

Images of the particle dispersion in the classroom for the DV and UFAD-CDR designs are shown in Figures 10 and 11 when the HVAC system is at full capacity. The diameter

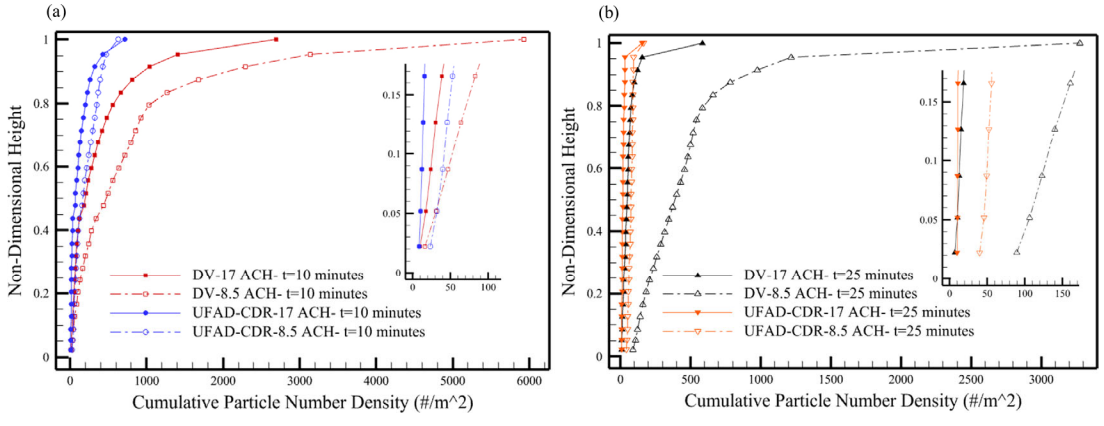

Fig. 9 Cumulative particle number densities in y direction for DV and UFAD-CDR designs at 17 and 8.5 ACHs: (a) at t = 10 minutes, (b) at t = 25 minutes

of the particles determines their colour in the figures. In less than five minutes, particles in the DV case reached the HVAC return-2 at the back side of the classroom. The 20 μm and larger particles only persist for about ten minutes in this situation, but 1 μm and 5 μm particles can still be found in the classroom 30 minutes after the lecturer stopped releasing them. Although 10 μm particles are not as persistent as those that are 5 μm and smaller, they could still travel far enough to be considered a potential risk of airborne transmission. As seen in Figure 11, particles have not spread far from the source, and all the students are safe in the UFAD-CDR ventilation design, in contrast to the baseline design where many of the students are at risk of being exposed to pathogens (Figure 10).

Figure 12 compares the particle suspension ratios for the DV and UFAD-CDR designs at 17 ACH to demonstrate how particle durability is influenced by particle size and ventilation design. The ventilation strategy has little impact on the suspension ratio of the 100 μm particles because they fall down immediately, but the suspension ratio of the

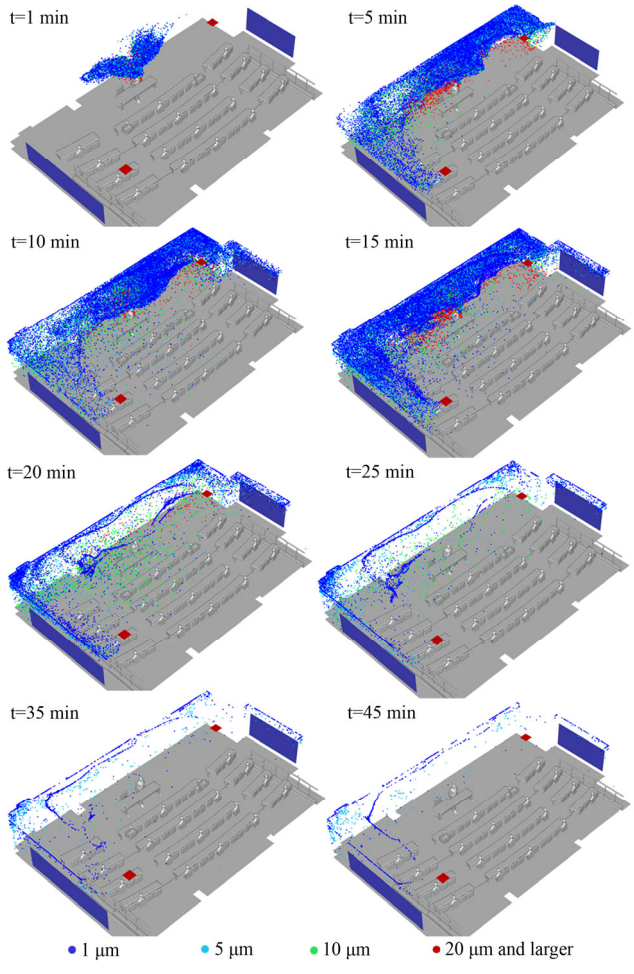

Fig. 10 Particle distributions in the classroom over 45 minutes-baseline design (DV) full HVAC load

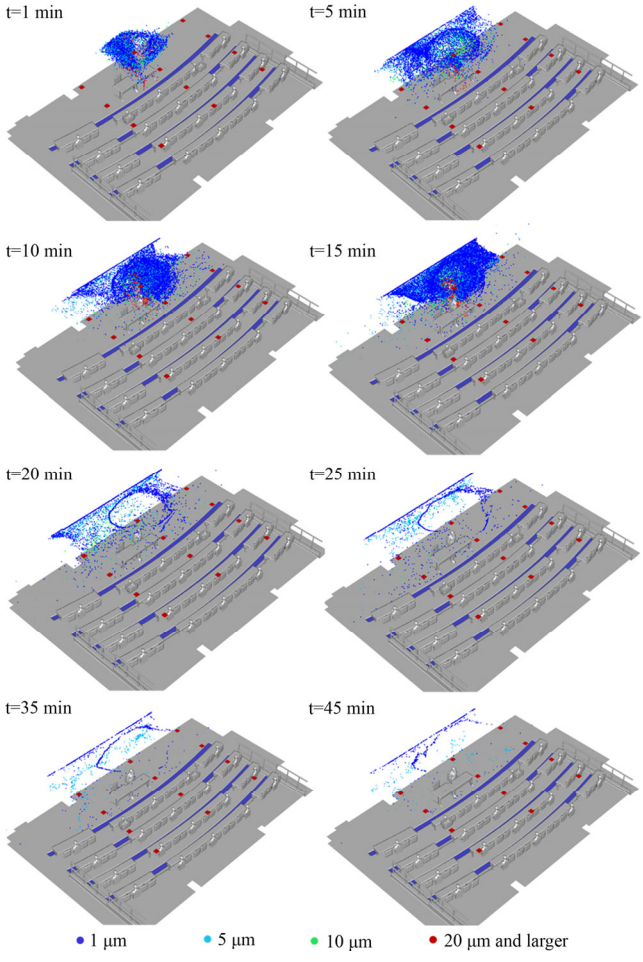

Fig. 11 Particle distributions in the classroom over 45 minutes-optimized design (UFAD-CDR) full HVAC load

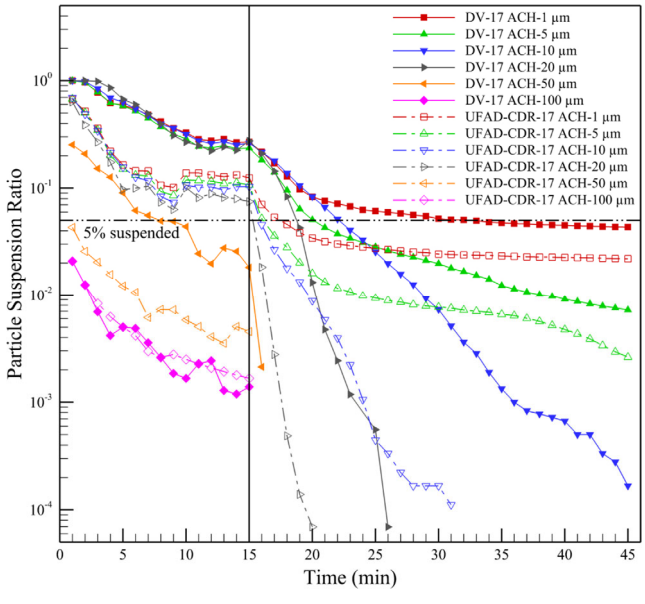

Fig. 12 Comparison of the particle suspension ratio (particle size breakdown) for the DV and UFAD-CDR designs at 17 ACH for 45 minutes

50 μm and smaller ones is significantly lower when the UFAD-CDR is in use. Although one and five micrometer particles can linger in the air for both ventilation designs even after 30 minutes of fallow time, the ratios for the UFAD-CDR layout drop below the 5% line in a few minutes, whereas the 5 μm and 1 μm particles drop below the 5% line in 6 and 19 minutes, respectively, when the baseline DV is used.

The energy-saving potential of the UFAD-CDR design becomes evident when compared to DV considering air quality in the classroom. Assuming a classroom consumes 200 kWh/m^2 a year, with 9% of the total energy dedicated to ventilation, 10% to cooling, and 47% to heating (Dias Pereira et al. 2014) our classroom's HVAC energy consumption rate is 23423 kWh per year (44.56 Wh per minute). When considering the necessary fallow time to remove 95% of emitted particles (2.5 minutes for UFAD-CDR and 19 minutes for the baseline DV) after five lectures per day, five days a week, and operating nine months of the year, the UFAD-CDR yields an energy savings of 661.8 kWh per year compared to the baseline DV just on shorter necessary fallow times. The suspended particles consistently remain significantly lower for the UFAD-CDR during the lectures, even at half flow rate (refer to Figure 8). During a pandemic, maximizing the intake of fresh air is recommended. In this condition, we can assume that the HVAC energy consumption is proportional to the flow rate. Reducing the flow rate by half, results in significant annual savings of 11711.5 kWh. UFAD-CDR design not only provides substantial cost savings (12373.3 kWh a year which is equivalent to 34.86% of total energy usage of the classroom) but also serves to improve air quality significantly, which is of vital importance during such critical periods.

5.4 Indoor airflow characteristics and aerosol transmission

Different flow characteristics, including vorticity, helicity, and enstrophy (Equations (9)–(11)) have been explored to quantify the flow pattern and discover an appropriate parameter that can indicate how high the risk of airborne transmission in a room could be by looking at the airflow. The magnitude and average of these parameters did not correlate with the particle distribution in the classroom; therefore, they may not be reliable indicators of the suitability of an airflow pattern.

Brownian diffusion is negligibly small in a turbulent flow (Ounis and Ahmadi 1990). The turbulent diffusion mechanism, which is caused by chaotic time-dependent motions, is distinct from the Brownian one. Aerosols would not be able to travel from a sick person to a susceptible one at a distance if there isn't any horizontal convectional flow and the Brownian motion is negligible. However, achieving such a flow pattern in a real room with all of the furniture and asymmetries present would be very difficult even if we were able to place uniform full-size HVAC supply and return underneath the floor and at the room's ceiling. Therefore, aerosols will inevitably be transported and carried by air in a horizontal direction as well.

A new parameter, horizontality, is introduced to compare the horizontal spread to the vertical transport of aerosols in indoor spaces, by determining how the large-scale flow pattern deviates from the ideal one-directional flow condition in a room. It can simply be defined as the ratio of two flow time scales in vertical, t_V, and horizontal, t_H, directions. These time scales are derived by dividing the room's length scales by the volume-averaged magnitudes of the horizontal and vertical velocity components:

$$t_V = \frac{\overline{h_R}}{\left(\sum V_i \left|u_{y,i}\right|\right)/V_R} \tag{14}$$

$$t_H = \frac{\sqrt{\overline{A_R}}}{\left(\sum V_i \sqrt{u_{x,i}^2 + u_{z,i}^2}\right)/V_R} \tag{15}$$

$$\bar{H} = \frac{t_V}{t_H} \tag{16}$$

where u_x and u_z are the horizontal components of the velocity vector, u_y is the vertical component of it, V_i is the computational cell volume and i is the cell number. $\overline{h_R}$ and $\overline{A_R}$ are the average height and cross-section area of the room and V_R is the room volume.

Figure 13 shows the horizontality level for various HVAC designs and flow rates. ACH has a minor impact on the horizontality level, and the horizontality of airflow in a room can quantify the large-scale flow pattern that plays a vital role in air quality in regard to airborne diseases transmission.

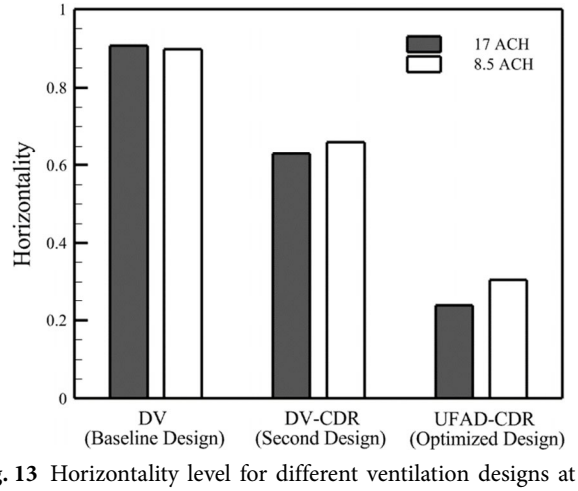

Fig. 13 Horizontality level for different ventilation designs at 17 and 8.5 ACHs

In order to integrate the impacts of ACH and large-scale flow patterns on the transmissibility of aerosols indoors and indicate how effectively an HVAC design can remove the aerosol particles, the normalized ACH on the horizontality level is defined as Equation (17) and called effective ACH (ACHH).

$$\mathrm{ACHH} = \frac{\mathrm{ACH}}{\overline{H}} \tag{17}$$

The ACHH values for six studied cases are provided in Table 4. The ACHH level provides a better descriptive value of the airborne particle's transmissibility than ACH and horizontality. The ACHH value for the worst case (baseline design-half load) is 9.45, and its value for the best case (optimized design-full load) is 71.47. The ACHH for the other cases is within these two values in a meaningful order related to the overall particle concentration in the classroom shown in Figure 8(a). Because the ACH role is not as important when the horizontality level is low for the UFAD-CDR case (see Figures 8(a) and 8(c)), ACHH may not be as accurate as it is for higher values of horizontality. The current standard codes primarily rely on the number of occupants and air quality expectations and thermal comfort but, as demonstrated in our study, that does not capture the substantial differences in air quality achieved under similar ACH conditions. Further multidisciplinary studies are needed to investigate the transmissibility of aerosols indoors in different scenarios to provide standard ACHH level suggestions, which account for both the flow rate and the ventilation design (flow pattern) based on the room occupancy categories.

In Figure 14, the velocity contours and streamlines for the DV and UFAD-CDR designs are compared in cutting through planes when the HVAC system is operating at full capacity. As it can be seen in Figures 14(a) and 14(b); the streamlines in the baseline design are oriented more in the horizontal direction than in the vertical direction. The airflow has been managed in the optimized design to reduce the horizontality of the circulating air, particularly where the

Table 4 ACHH

Case	DV 17 ACH	DV 8.5 ACH	DV-CDR 17 ACH	DV-CDR 8.5 ACH	UFAD-CDR 17 ACH	UFAD-CDR 8.5 ACH
ACHH	18.75	9.45	27.01	12.86	71.47	27.83

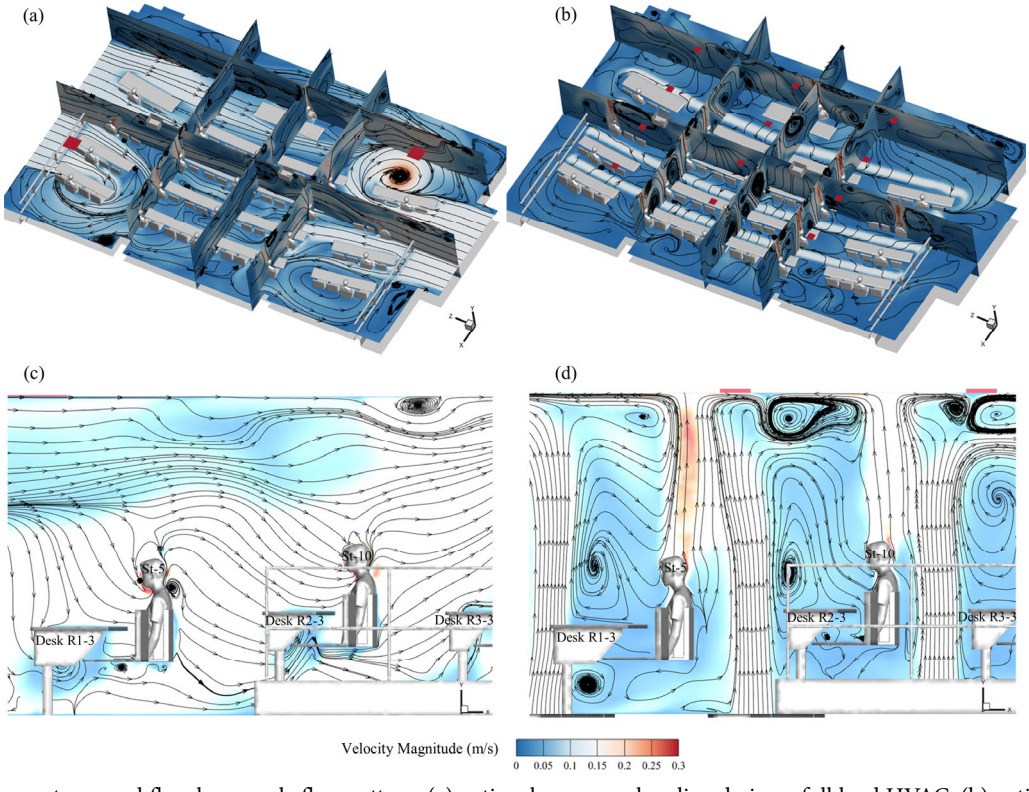

Fig. 14 Velocity contours and flow large-scale flow pattern: (a) entire classroom—baseline design—full load HVAC; (b) entire classroom—optimized design—full load HVAC; (c) St-5 and St-10—baseline design—full load HVAC; (d) St-5 and St-10—optimized design—full load HVAC

student seats are located. More rows of air supplies and returns could be added to help control the airflow at the classroom corners. Figures 14(c) and 14(d) compare the velocity contours and airflow large-scale patterns around St-5 and St-10 for the baseline and optimized designs. In the controlled circulation scenario, students breathe in their own local airflow circulation bubbles which can significantly reduce the risk of airborne disease transmission. While in the baseline design, an aerosol would easily be carried by the background flow from one student to another if it had to travel on the shown cutting plane.

5.5 Aerosol source location test

Two additional simulations for the DV and UFAD-CDR designs were performed to evaluate the effects of particle source location on the efficacy of the optimized design. Instead of the lecturer, one of the students (St-8) in the middle of the classroom generates particles for 15 minutes. Figure 15 compares the distribution of the particles in the classroom for these cases at 10 and 20 minutes from the start of the simulations. The particles are coloured by their position in y direction. For the DV design at t = 10 minutes (Figure 15(a)), 25.89% of the released particles are still present in the computational domain and are wildly spread in the classroom while only 3.83% of the particles are suspended mainly in close proximity to the St-8 at this time (Figure 15(b)). When UFAD-CDR ventilation is used, only 196 particles (0.08%) remain suspended in the air at t = 20 minutes (5 minutes of fallow time), whereas 14,509 particles (5.92%) are still present in the classroom when the DV is used. The findings show that the UFAD-CDR design is significantly safer than DV in both emission and fallow time, regardless of where the infected person is located.

6 Conclusions

A real university classroom has been considered for numerically investigating aerosol and particle transport when people are present indoors. Unsteady simulations were performed for 45 minutes under various background airflow conditions, ACHs, and human thermal effects. A new parameter called "horizontality" has been introduced to quantify and link the large-scale flow pattern to the transmission of airborne diseases. This study presents a classroom ventilation layout (UFAD-CDR) that can efficiently remove aerosols in a relatively short period of time under varied ACHs. The following are the study's key findings:

The particle size threshold at which particles become airborne is heavily influenced by the strength and large-scale flow pattern of the background flow. It could be 5–10 μm in the cases under consideration. Although 20 μm particles can travel several meters, they do not last long in the air.

Human respiratory particle transport studies must take into account the significant effects of human presence on indoor aerosol transport, particularly the thermally buoyant flow effect that creates a thermal plume around people.

A 10-minute break does not guarantee that the following lecture will begin in a safe environment unless the ventilation is designed for aerosol transmission control.

When it comes to the transmission of airborne diseases, air quality cannot be controlled solely by a certain amount

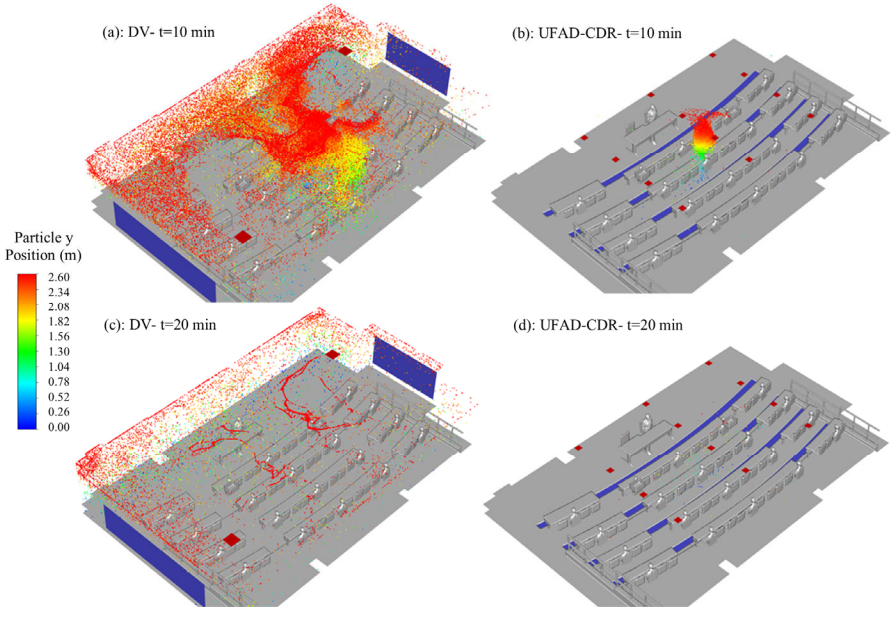

Fig. 15 Particle distribution in the classroom under DV and UFAD-CDR ventilations, when a student in the middle of the classroom emits particles

of air change per hour (ACH). The large-scale airflow pattern is another critical factor. It has been found that measuring the airflow's horizontality is an effective method for determining how well the air circulation in a room contributes to the prevention of airborne disease spread.

Because each room has a different large-scale airflow pattern based on room and ventilation designs, standard codes should be adequately revised to define an appropriate ACH level alongside the horizontality for each occupancy type. However, further research needs to be conducted to investigate horizontality and provide effective ACH (ACHH) charts for varied room occupancy applications.

At lower ACHs, aerosols may be concentrated near the floor if they have enough time to settle. The development of the thermal plume in a room with displacement ventilation pulls air up to the breathing zone from the lower parts of the room. A higher ACH would contribute to a safer environment by preventing particles, in prolonged activities with sedentary people, from accumulating near the floor.

An under-floor air distribution concept combined with a ceiling-distributed returns ventilation layout (UFAD-CDR) provides a large-scale airflow pattern with a low horizontality level for university classrooms. Compared to conventional displacement ventilation systems, the UFAD-CDR dramatically reduces the probability of airborne transmission at both high and low ACHs.

Acknowledgements

This research was supported by the Airborne Disease Transmission Research Cluster (ADTRC), which is funded by the UBC Eminence program. The authors gratefully acknowledge the use of Digital Research Alliance of Canada resources for CFD simulations.

Declaration of competing interest

The authors have no competing interests to declare that are relevant to the content of this article.

References

Abrahamson J (2021). Fluent Theory Guide. 1068.

Abuhegazy M, Talaat K, Anderoglu O, et al. (2020). Numerical investigation of aerosol transport in a classroom with relevance to COVID-19. *Physics of Fluids*, 32: 103311.

Al Assaad D, Ghali K, Ghaddar N (2019). Particles dispersion due to human prostration cycle and ventilation system in a prayer room. *Building and Environment*, 150: 44–59.

Alsved M, Matamis A, Bohlin R, et al. (2020). Exhaled respiratory particles during singing and talking. *Aerosol Science and Technology*, 54: 1245–1248.

Anfinrud P, Stadnytskyi V, Bax CE, et al. (2020). Visualizing speech-generated oral fluid droplets with laser light scattering. *The New England Journal of Medicine*, 382: 2061–2063.

Arjmandi H, Amini R, Khani F, et al. (2022). Minimizing the respiratory pathogen transmission: numerical study and multi-objective optimization of ventilation systems in a classroom. *Thermal Science and Engineering Progress*, 28: 101052.

Brohus H, Nielsen PV (1996). Personal exposure in displacement ventilated rooms. *Indoor Air*, 6: 157–167.

Chan TL, Dong G, Leung CW, et al. (2002). Validation of a two-dimensional pollutant dispersion model in an isolated street canyon. *Atmospheric Environment*, 36: 861–872.

Chen C, Zhao B (2010). Some questions on dispersion of human exhaled droplets in ventilation room: answers from numerical investigation. *Indoor Air*, 20: 95–111.

Chen C, Zhao B, Weschler CJ (2012). Indoor exposure to "outdoor PM_{10}". *Epidemiology*, 23: 870–878.

Dias Pereira L, Raimondo D, Corgnati SP, et al. (2014). Energy consumption in schools—A review paper. *Renewable and Sustainable Energy Reviews*, 40: 911–922.

Gao NP, Niu JL (2007). Modeling particle dispersion and deposition in indoor environments. *Atmospheric Environment*, 41: 3862–3876.

Gao N, Niu J, He Q, et al. (2012). Using RANS turbulence models and Lagrangian approach to predict particle deposition in turbulent channel flows. *Building and Environment*, 48: 206–214.

Gao R, Li A (2012). Dust deposition in ventilation and air-conditioning duct bend flows. *Energy Conversion and Management*, 55: 49–59.

Gupta JK, Lin C-H, Chen Q (2010). Characterizing exhaled airflow from breathing and talking. *Indoor Air*, 20: 31–39.

Hassan AM, Megahed NA (2021). COVID-19 and urban spaces: A new integrated CFD approach for public health opportunities. *Building and Environment*, 204: 108131.

Hendiger J, Chludzińska M, Ziętek P (2016). Influence of the pressure difference and door swing on heavy contaminants migration between rooms. *PLoS One*, 11: e0155159.

Jayaweera M, Perera H, Gunawardana B, et al. (2020). Transmission of COVID-19 virus by droplets and aerosols: a critical review on the unresolved dichotomy. *Environmental Research*, 188: 109819.

Klepeis NE, Nelson WC, Ott WR, et al. (2001). The National Human Activity Pattern Survey (NHAPS): a resource for assessing exposure to environmental pollutants. *Journal of Exposure Science & Environmental Epidemiology*, 11: 231–252.

Kohanski MA, Lo LJ, Waring MS (2020). Review of indoor aerosol generation, transport, and control in the context of COVID-19. *International Forum of Allergy & Rhinology*, 10: 1173–1179.

Leung NHL (2021). Transmissibility and transmission of respiratory viruses. *Nature Reviews Microbiology*, 19: 528–545.

Li Y, Leung GM, Tang JW, et al. (2007). Role of ventilation in airborne transmission of infectious agents in the built environment? A multidisciplinary systematic review. *Indoor Air*, 17: 2–18.

Li X, Niu J, Gao N (2013). Co-occupant's exposure to exhaled pollutants with two types of personalized ventilation strategies under mixing and displacement ventilation systems. *Indoor Air*, 23: 162–171.

Li J, Cao X, Liu J, et al. (2018). PIV measurement of human thermal convection flow in a simplified vehicle cabin. *Building and Environment*, 144: 305–315.

Li Y, Wang J, Chen X (2020). Can a toilet promote virus transmission? From a fluid dynamics perspective. *Physics of Fluids*, 32: 065107.

Li P, Liu W, Zhang TT (2023). CFD modeling of dynamic airflow and particle transmission in an aircraft lavatory. *Building Simulation*, 16: 1375–1390.

Liu Y, Wang L, Di Y, et al. (2013). The effects of clothing thermal resistance and operative temperature on human skin temperature. *Journal of Thermal Biology*, 38: 233–239.

Liu Z, Liu H, Rong R, et al. (2020). Effect of a circulating nurse walking on airflow and bacteria-carrying particles in the operating room: An experimental and numerical study. *Building and Environment*, 186: 107315.

Liu Z, Wu M, Cao H, et al. (2021). Influence of the visitor walking on airflow and the bioaerosol particles in typical open tomb chambers: an experimental and case study. *Buildings*, 11: 538.

Mirzaie M, Lakzian E, Khan A, et al. (2021). COVID-19 spread in a classroom equipped with partition - A CFD approach. *Journal of Hazardous Materials*, 420: 126587.

Morawska L (2006). Droplet fate in indoor environments, or can we prevent the spread of infection? *Indoor Air*, 16: 335–347.

Morawska L, Johnson GR, Ristovski ZD, et al. (2009). Size distribution and sites of origin of droplets expelled from the human respiratory tract during expiratory activities. *Journal of Aerosol Science*, 40: 256–269.

Morawska L, Tang JW, Bahnfleth W, et al. (2020). How can airborne transmission of COVID-19 indoors be minimised? *Environment International*, 142: 105832.

Ounis H, Ahmadi G (1990). A comparison of Brownian and turbulent diffusion. *Aerosol Science and Technology*, 13: 47–53.

Pendar MR, Páscoa JC (2020). Numerical modeling of the distribution of virus carrying saliva droplets during sneeze and cough. *Physics of Fluids*, 32: 083305.

Phuong NL, Yamashita M, Yoo S-J, et al. (2016). Prediction of convective heat transfer coefficient of human upper and lower airway surfaces in steady and unsteady breathing conditions. *Building and Environment*, 100: 172–185.

Ramponi R, Blocken B (2012). CFD simulation of cross-ventilation for a generic isolated building: impact of computational parameters. *Building and Environment*, 53: 34–48.

Rencken GK, Rutherford EK, Ghanta N, et al. (2021). Patterns of SARS-CoV-2 aerosol spread in typical classrooms. *Building and Environment*, 204: 108167.

Rogak SN, Rysanek A, Lee JM, et al. (2022). The effect of air purifiers and curtains on aerosol dispersion and removal in multi-patient hospital rooms. *Indoor Air*, 32: e13110.

Romano F, Marocco L, Gustén J, et al. (2015). Numerical and experimental analysis of airborne particles control in an operating theater. *Building and Environment*, 89: 369–379.

Saarinen PE, Kalliomäki P, Tang JW, et al. (2015). Large eddy simulation of air escape through a hospital isolation room single hinged doorway—Validation by using tracer gases and simulated smoke videos. *PLoS One*, 10: e0130667.

Shahdad S, Hindocha A, Patel T, et al. (2021). Fallow time determination in dentistry using aerosol measurement in mechanically and non-mechanically ventilated environments. *British Dental Journal*: 1–8.

Tang Y, Guo B, Ranjan D (2015). Numerical simulation of aerosol deposition from turbulent flows using three-dimensional RANS and LES turbulence models. *Engineering Applications of Computational Fluid Mechanics*, 9: 174–186.

Tao Y, Inthavong K, Tu JY (2017). Dynamic meshing modelling for particle resuspension caused by swinging manikin motion. *Building and Environment*, 123: 529–542.

Thatiparti DS, Ghia U, Mead KR (2017). Computational fluid dynamics study on the influence of an alternate ventilation configuration on the possible flow path of infectious cough aerosols in a mock airborne infection isolation room. *Science and Technology for the Built Environment*, 23: 355–366.

Tominaga Y, Stathopoulos T (2009). Numerical simulation of dispersion around an isolated cubic building: comparison of various types of k-ε models. *Atmospheric Environment*, 43: 3200–3210.

Tung Y-C, Shih Y-C, Hu S-C (2009). Numerical study on the dispersion of airborne contaminants from an isolation room in the case of door opening. *Applied Thermal Engineering*, 29: 1544–1551.

Vuorinen V, Aarnio M, Alava M, et al. (2020). Modelling aerosol transport and virus exposure with numerical simulations in relation to SARS-CoV-2 transmission by inhalation indoors. *Safety Science*, 130: 104866.

Wang H, Lin M, Chen Y (2014). Performance evaluation of air distribution systems in three different China railway high-speed train cabins using numerical simulation. *Building Simulation*, 7: 629–638.

Wang C, Holmberg S, Sadrizadeh S (2021a). Impact of door opening on the risk of surgical site infections in an operating room with mixing ventilation. *Indoor and Built Environment*, 30: 166–179.

Wang J-X, Cao X, Chen Y-P (2021b). An air distribution optimization of hospital wards for minimizing cross-infection. *Journal of Cleaner Production*, 279: 123431.

Wu Q, Liu J, Zhang L, et al. (2020). Effect of temperature and clothing thermal resistance on human sweat at low activity levels. *Building and Environment*, 183: 107117.

Xu S, Zhang G, Liu X, et al. (2023). CFD modelling of infection control in indoor environments: A focus on room-level air recirculation systems. *Energy and Buildings*, 288: 113033.

Yan W, Zhang Y, Sun Y, et al. (2009). Experimental and CFD study of unsteady airborne pollutant transport within an aircraft cabin mock-up. *Building and Environment*, 44: 34–43.

Yang C, Liu J, He F (2017). Evolution of large-scale flow structures and traces of marked fluid particles within a single-aisle cabin mock-up. *Building Simulation*, 10: 723–736.

Yang Y, Wang Y, Tian L, et al. (2022). Effects of purifiers on the airborne transmission of droplets inside a bus. *Physics of Fluids*, 34: 017108.

Yu ITS, Li Y, Wong TW, et al. (2004). Evidence of airborne transmission of the severe acute respiratory syndrome virus. *New England Journal of Medicine*, 350: 1731–1739.

Yu H, Thé J (2017). Simulation of gaseous pollutant dispersion around an isolated building using the k-ω SST (shear stress transport) turbulence model. *Journal of the Air & Waste Management Association*, 67: 517–536.

Zabihi M, Li R, Brinkerhoff J, et al. (2022). Numerical investigation of aerosol transmission in a Classroom. In: Proceedings of the Canadian Society for Mechanical Engineering International Congress 2022, Edmonton, Canada.

Zhang Z, Wang Y, Li J (2010). Mathematical simulation and experimental measurement of clothing surface temperature under different sized air gaps. *Fibers and Polymers*, 11: 911–916.

Zhao B, Zhang Z, Li X (2005). Numerical study of the transport of droplets or particles generated by respiratory system indoors. *Building and Environment*, 40: 1032–1039.

Zukowska D, Melikov A, Popiolek Z (2012). Impact of geometry of a sedentary occupant simulator on the generated thermal plume: Experimental investigation. *HVAC&R Research*, 18: 795–811.